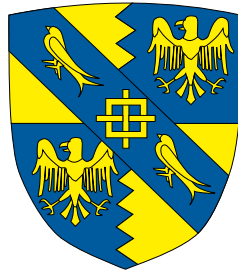


Light-sheet microscopy used for tracking particles



Craig T. Russell

Department of Chemical Engineering and Biotechnology
University of Cambridge

This dissertation is submitted for the degree of
Doctor of Philosophy

Magdalene College

September 2018

Declaration

I hereby declare that except where specific reference is made to the work of others, the contents of this dissertation are original and have not been submitted in whole or in part for consideration for any other degree or qualification in this, or any other university. This dissertation is my own work and contains nothing which is the outcome of work done in collaboration with others, except as specified in the text and Acknowledgements. This dissertation contains fewer than 65,000 words including appendices, bibliography, footnotes, tables and equations and has fewer than 150 figures.

Craig T. Russell
September 2018

Acknowledgements

And I would like to acknowledge ...

Abstract

Fluorescence microscopy is one of the cornerstones of modern biology, but has generally been limited to 2D culture dishes. Light-sheet microscopy, a recent advance which was awarded Nature Method of the Year 2014, allows fast, non-invasive 3D imaging across an entire organism. This works by decoupling illumination and detection such that the microscope only illuminates a thin section of tissue at a time. By scanning this 'light-sheet' through an organism we can image in 3D, more quickly and with less damage than other techniques such as confocal microscopy.

In this work a custom light-sheet microscope was built which was have applied to studying the cell mechanics of developing embryos. Internal stresses within tissues induce cellular migrations that can govern the organism's resultant anatomy. A technique was developed to mechanically probe deep tissue using magnetism. By embedding a magnetic bead in an embryo we can use a controllable, non-invasive magnetic field to move the bead. By pushing a magnetic

bead and allowing it to relax we can fit a model to its trajectory and so extract local mechanical properties. The mechanical roles of key proteins in embryonic development can be inferred by comparing results between genetically modified embryos. Our investigations so far have contradicted previous reports that rho-kinase increases cell stiffness in embryonic development. These results are currently being prepared for publication with our collaborators.

The scope of three dimensional tracking was moved from going from the microscopic (tracking a single magnetic beads) to nanoscopic scale by to tracking virus particles (virions) which invade host cells and hijack their machinery to replicate and then spread. By visualising the journey of virions through the cell we may reveal weaknesses in infection pathways. Light-sheet microscopy is better suited than other techniques for tracking virus trafficking in 3D as virions are exceptionally small and fast. Herpes Simplex Virus 1 was studied which is the widespread cause of cold sores and gen-

ital herpes. Furthermore, it serves as a biological model for other Herpesviruses which are associated with many serious diseases including chickenpox and certain lymphomas.

In addition to designing and constructing a light-sheet fluorescence microscope technological improvements were investigated: The first was a three dimensional region-of-interest technique which promises to simultaneously simplify volumetric imaging calibration whilst being more robust than current approaches. The second improvement builds upon confocal slit scanning, a technique used

to increase image contrast whilst doubling the acquisition time for a single image. This development allowed for full speed imaging with the same increased contrast.

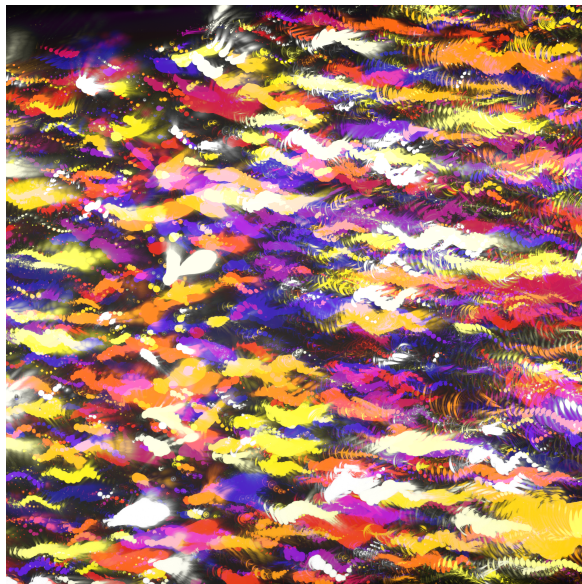


Image of beads drifting through the focal plane of the light-sheet microscope where colour encodes time

Table of contents

List of figures	xv
List of tables	xvii
Glossary	xix
Acronyms	xxi
Appendix A Appendixed Methods	1
A.1 Measuring focal length of scan lens	1
A.2 System alignments protocol	2
A.3 Convolution Theorem	2
A.4 Fourier transform	4
A.5 Huygens	5
Appendix B Particle tracking	7
B.1 Failed quantifications of motion induced error	7
B.1.1 Cross correlation	7
B.1.2 Full width half maximum	9
B.2 Bragg conditons	10

List of figures

A.1	Laser Width Fitting	3
B.1		8

List of tables

Glossary

light-sheet A thin plane of light 1, 3

Acronyms

AFM Atomic Force Microscopy 2

EM Electron Microscopy 2

HSV Herpes Simplex Virus 2

Appendix A

Appendixed Methods

A.1 Measuring focal length of scan lens

The focal length of the scan lens was initially unknown but its position for collimation was, and so a reasonable assumption of its focal length was possible. To compound certainty the focal length was found experimentally. To accurately measure the focal length of an unknown lens the focal length of a lens of known focal length is needed to collimate the light. In this experiment the tube lens of focal length 200 mm was used. By measuring the width of a laser beam prior (w_{before}) to and after (w_{after}) the collimating lens pair, the magnification is calculated very accurately and the unknown focal length is found by:

$$M = \frac{f_2}{f_1} = \frac{w_{before}}{w_{after}} \rightarrow \frac{f_2}{M} = f_1 \quad (\text{A.1})$$

To measure a beam width very accurately a straight sharp edge is placed in the beam path and slowly iterated through, the resultant beam power is then measured using a power meter. To ensure there is no beam cropping on the power meter another lens was used to focus the intensity correctly, the same lens and its position was used in each measurement to keep with consistency. The beam power was measured and plotted which produces an integrated Gaussian profile (see (A.2)) otherwise known as an error function. Mathematically this is described by equation (A.3).

$$I(x, y) = I_0 e^{\frac{-2x^2}{w_x^2}} e^{\frac{-2y^2}{w_y^2}} \quad (\text{A.2})$$

$$\begin{aligned} P_{TOT} &= I_0 \int_{-\infty}^{\infty} e^{\frac{-2x^2}{w_x^2}} dx \int_{-\infty}^{\infty} e^{\frac{-2y^2}{w_y^2}} dy \\ P(X) &= P_{TOT} - \int_{-\infty}^X e^{\frac{-2x^2}{w_x^2}} dx I_0 \int_{-\infty}^{\infty} e^{\frac{-2y^2}{w_y^2}} dy \\ &= \frac{P_{TOT}}{2} - \sqrt{\frac{\pi}{2}} I_0 \omega_y \int_{-\infty}^X e^{\frac{-2x^2}{w_x^2}} dx \\ &= \frac{P_{TOT}}{2} \left[1 - \operatorname{erf} \left(\frac{\sqrt{2}X}{\omega_x} \right) \right] \end{aligned} \quad (\text{A.3})$$

Fitting of this curve was implemented using MatLAB's curve fitting package which utilises the method of least squares fitting, see Figure ???. The fit result produced values of laser beam width as $w_{before} = 3.76 \pm 0.04$ mm and $w_{after} = 0.71 \pm 0.10$ mm. The value of w_{after} was supplied in Table ?? however, for posterity it was remeasured locally in case the value had changed or was incorrect. This gives a magnification M of 5.37 ± 0.10 therefore the focal length of the scan lens is 37.3 ± 0.1 mm. This also showed that the fill of the 12 mm back aperture was 3.76 ± 0.04 mm hence the NA of the 0.3 objective used would be ≈ 0.094 .

A.2 System alignments protocol

A.3 Convolution Theorem

Convolution is a mathematical operation between two functions, say $g(t)$ and $f(t)$, with the resultant function being an expression of the overlap of g as it is shifted over f [Bracewell1921-]. Mathematically it can be expressed as an integral over a finite range τ :

$$[f(*g)](t) = \int_{-\infty}^{\infty} f(\tau) g(t - \tau) d\tau \quad (\text{A.4})$$

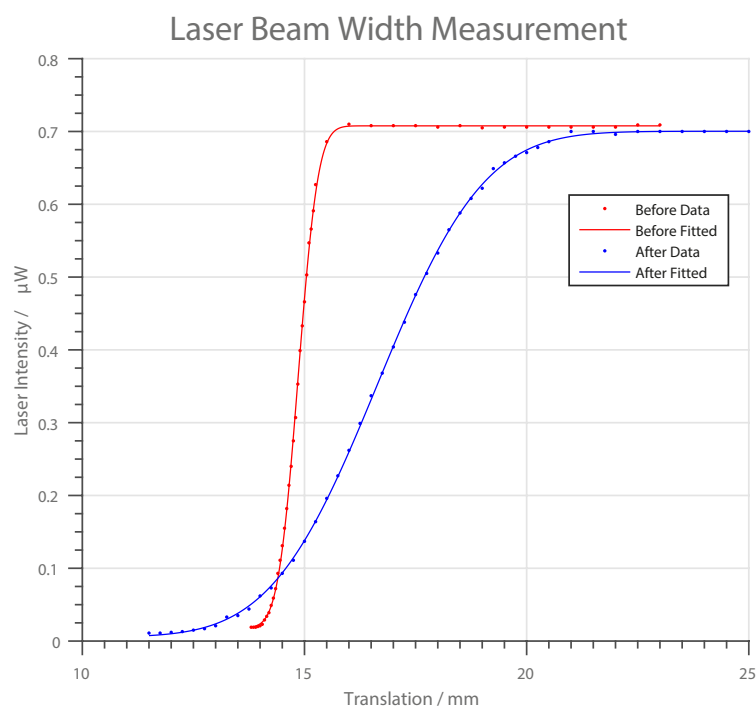


Fig. A.1 Plot showing the fitting of two error functions based on the knife edge translation through a laser beam propagation, producing laser beam widths of $w_{\text{after}} = 0.71 \pm 0.10 \text{ mm}$ and $w_{\text{before}} = 3.76 \pm 0.04 \text{ mm}$

If a Fourier transform is then applied to the convolution of two functions:

$$\mathcal{F}([f * g](t)) = \int_{-\infty}^{\infty} \left[\int_{-\infty}^{\infty} f(\tau)g(t - \tau)d\tau \right] e^{-i2\pi kt}dt \quad (\text{A.5})$$

and then reverse the order:

$$\mathcal{F}([f * g](t)) = \int_{-\infty}^{\infty} f(\tau) \left[\int_{-\infty}^{\infty} g(t - \tau)e^{-i2\pi kt}dt \right] d\tau \quad (\text{A.6})$$

From the shift theorem seen in equation (A.12):

$$\left[\int_{-\infty}^{\infty} g(t - \tau)e^{-i2\pi kt}dt \right] = \mathcal{F}(g(t - \tau)) = \mathcal{F}(g(t))e^{-i2\pi k\tau} \quad (\text{A.7})$$

$$\implies \mathcal{F}([f * g](t)) = \mathcal{F}(g(t)) \int_{-\infty}^{\infty} f(\tau)e^{-i2\pi k\tau}d\tau \quad (\text{A.8})$$

$$= \mathcal{F}(g(t))\mathcal{F}(f(\tau)) \quad (\text{A.9})$$

Showing that **Convolution** in real space is **Multiplication** in Fourier space.

A.4 Fourier transform

Any continuous function can be decomposed into a linear summation of harmonic weighted sinusoidal functions. A Fourier transform is a mechanism by which the weightings of this series can be derived. Fourier space uses this transform to represent a function or a signal in frequency space (sometimes known as k -space or reciprocal space); it can be seen as a coordinate change from x to k denoted mathematically as: [Bloomfield1946]

$$F(k) \equiv \mathcal{F}\{f(x)\} \equiv \int_{-\infty}^{\infty} f(x)e^{-i2\pi kx}dx \quad (\text{A.10})$$

This process is also reversible by:

$$f(x) \equiv \mathcal{F}^{-1}\{F(k)\} \equiv \frac{1}{2\pi} \int_{-\infty}^{\infty} F(k)e^{-i2\pi kx}dk \quad (\text{A.11})$$

Fourier transforms have a valuable property in that a shift in real space becomes a complex phase term in k space. This is shown by substituting $x = x - a$ and $dx = dx$

into (A.10):

$$\begin{aligned} F(k') &= \int_{-\infty}^{\infty} f(x) e^{-i2\pi k(x-a)} dx \\ &= e^{-i2\pi ka} \underbrace{\int_{-\infty}^{\infty} f(x) e^{-i2\pi kx} dx}_{F(k)} \end{aligned} \quad (\text{A.12})$$

Hence the additional real space shift only adds a multiplicative factor to the final Fourier transform. This is known as the Shift theorem.

A.5 Huygens

Diffraction is the spreading of light rays after an interaction with an object. Coincident light waves may interfere when diffracted such that the superposition of their resultant waves is constructive or destructive dependent on their relative phase difference. Light incident on an aperture $A(x, y)$ in the plane S can be assumed to be of a plane wave nature. When passing through the aperture, light can then be modelled as being a series of dS spaced point sources that radiate spherical wavefronts under Huygens' principle:

"Every point on a propagating wavefront serves as the source of secondary spherical wavelets, such that the wavefront at some later time is the envelope of these wavelets." [Goodman2005]

The superposition and hence summation of these emitting wavelets when only travelling forward ($+z$ direction) and contained in a cone of small angles from the optical axis can be evaluated in terms of dE , the change in the field at some point in front of the aperture. The change in field goes with $\frac{1}{r}$ where r represents the distance to an arbitrary point and for a real wave can be expressed as:

$$dE = \frac{A(x, y)dS}{r} \cos(\omega t - kr) \quad (\text{A.13})$$

Using the coordinates α, β to represent the two dimensional plane of the projection of the light passing through the aperture $A(x, y)$ then r and R can be written as:

$$R^2 = \alpha^2 + \beta^2 + z^2 \quad (\text{A.14})$$

$$r^2 = (\alpha - x)^2 + (\beta - y)^2 + z^2 \quad (\text{A.15})$$

Where R represents the distance from the optical centre of the aperture to the arbitrary point at α, β , which can be rewritten as:

$$r = R \sqrt{1 - \frac{2\alpha x + 2\beta y}{R^2} + \frac{x^2 + y^2}{R^2}} \quad (\text{A.16})$$

Which can be approximated using a binomial expansion to:

$$r = R - \frac{(\alpha x + \beta y)}{R} \quad (\text{A.17})$$

Provided the cone of angles is small, then $r \approx R$ and when only considering the case where $R^2 \gg x^2 + y^2$ equation (A.16) tends to:

$$dE = \frac{A(x, y)}{R} e^{i\omega t - kr} e^{ik\left(\frac{\alpha x + \beta y}{R}\right)} dx dy \quad (\text{A.18})$$

Integrating across the entire aperture (wavefronts are entirely rejected elsewhere):

$$E(\alpha, \beta) = \frac{e^{i\omega t - kr}}{R} \int \int_A A(x, y) e^{ik\left(\frac{\alpha x + \beta y}{R}\right)} dx dy \quad (\text{A.19})$$

After a normalised coordinate switch:

$$u = \frac{k\alpha}{2\pi R} \text{ and } v = \frac{k\beta}{2\pi R} \quad (\text{A.20})$$

$$E(u, v) = \frac{e^{i\omega t - kr}}{R} \int \int_A A(x, y) e^{i2\pi k(ux + vy)} dx dy \quad (\text{A.21})$$

This form is well known and defined as a Fourier transform (with a weighting term) and hence the far field diffraction pattern of an aperture is the Fourier transform of that aperture [Goodman2005].

Appendix B

Particle tracking

B.1 Failed quantifications of motion induced error

Introduced in section ??, attempts at quantify the error seen due to motion blur that failed.

B.1.1 Cross correlation

To analytically compare the expected and real results, the respective functions were cross-correlated using the analytical function:

$$(f \star g)(t) \stackrel{\text{def}}{=} \int_{-\infty}^{\infty} f(x)^* g(x + t) dx$$

The integral of the result across all space gives a single value signifying the quality of correlation between the two functions:

$$\int_{-\infty}^{\infty} \int_{-\infty}^{\infty} f(t)^* g(x + t) dx dt$$

This value will reach unity when $f(x) = g(x)$

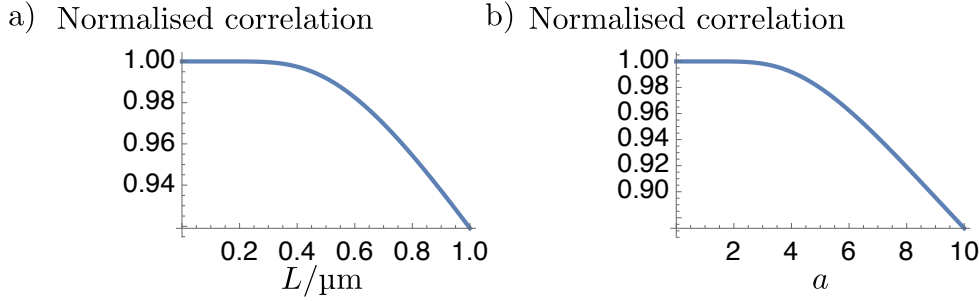


Fig. B.1

The expected PSF was given the additional t parameter as it was more likely that this integral would solve, though, this only solves across all space for unnormalised PSFs:

$$\begin{aligned} & \int_{-\infty}^{\infty} \int_{-\infty}^{\infty} \text{PSF}_{\text{Reality}}(x)^* \text{PSF}_{\text{Expected}}(x+t) dx dt \\ &= \frac{\pi c(aL + L_{\text{end}})^2}{aL_{\text{end}}L\sqrt{\frac{L_{\text{end}}^2}{c^2(aL+L_{\text{end}})^2}}} + \frac{2\pi c^2(aL + L_{\text{end}})^2}{L_{\text{end}}^2} \\ &+ \frac{\pi cL_{\text{end}}}{aL\sqrt{\frac{L_{\text{end}}^2}{c^2(aL+L_{\text{end}})^2}}} - \frac{2\pi L_{\text{end}}}{a\sqrt{\frac{1}{c^2}\sqrt{\frac{L_{\text{end}}^2}{c^2(aL+L_{\text{end}})^2}}}} \\ &+ \frac{2\pi c^2(aL + L_{\text{end}})^2}{aL_{\text{end}}L} \end{aligned}$$

By correlating the normalised functions across a small window u an analytical solution was produced.

$$\begin{aligned} & \int_{-u}^u \int_{-\infty}^{\infty} \hat{\text{PSF}}_{\text{Reality}}(x)^* \hat{\text{PSF}}_{\text{Expected}}(x+t) dx dt \\ &= -\frac{(aL + L_{\text{end}})}{\sqrt{2\pi}aL_{\text{end}}L} \sqrt{\frac{L_{\text{end}}^2}{c^2(aL+L_{\text{end}})^2}} \left(L_{\text{end}}u \left(\text{Ei} \left(-\frac{L_{\text{end}}^2 u^2}{2c^2(L_{\text{end}} + aL)^2} \right) + \Gamma \left(0, \frac{u^2}{2c^2} \right) \right) \right. \\ & \quad \left. - \frac{\sqrt{2\pi(-c)}(aL + L_{\text{end}}) \left(\text{Erf} \left(\frac{L_{\text{end}}u}{\sqrt{2}(acL+cL_{\text{end}})} \right) \right)}{\sqrt{2\pi}aL_{\text{end}}L} - \frac{\sqrt{2\pi}L_{\text{end}}|c| \text{Erf} \left(\frac{u}{\sqrt{2}|c|} \right)}{\sqrt{2\pi}aL_{\text{end}}L} \right) \end{aligned}$$

B.1.2 Full width half maximum

The correlation of two signals is not an absolute error which can be used to make predictions about real-world systems. So, the Full Width at Half Maximum of each of the two signals was considered as this property, in Gaussian-like functions, should provide an analogue for $\sigma(z)$ which may be compared absolutely.

$$\begin{aligned} \text{PSF}(x, \dots) - \lim_{x \rightarrow 0} \frac{\text{PSF}(x, \dots)}{2} &= 0 \\ \implies \text{FWHM}_{\text{Expected}} &= 2x \\ &= \left| -\frac{\sqrt{2c}\sqrt{\ln 2 + 2i\pi n}(aL + L_{\text{end}})}{L_{\text{end}}} \right|, n \in \mathbb{Z} \end{aligned}$$

$$\text{PSF}_{\text{Reality}}(x, \dots) - \lim_{x \rightarrow 0} \frac{\text{PSF}_{\text{Reality}}(x, \dots)}{2} = 0$$

This equation does not solve for x so a Maclaurin expansion was used:

$$= -\frac{L_{\text{end}}x^2}{4(c^2(aL + L_{\text{end}}))} + \frac{x^4(a^2L_{\text{end}}L^2 + 3aL_{\text{end}}^2L + 3L_{\text{end}}^3)}{48c^4(aL + L_{\text{end}})^3} + O(x^5)$$

$$\begin{aligned} \implies \text{FWHM}_{\text{Reality}} &= \frac{2\sqrt{3}}{\sqrt{\frac{a^2L^2}{c^2(aL + L_{\text{end}})^2} + \frac{3L_{\text{end}}^2}{c^2(aL + L_{\text{end}})^2} + \frac{3aL_{\text{end}}L}{c^2(aL + L_{\text{end}})^2}}} \\ \text{FWHM}_{\text{Error}} &= 2 \frac{\text{PSF}_{\text{Expected}} - \text{PSF}_{\text{Reality}}}{\text{PSF}_{\text{Expected}} + \text{PSF}_{\text{Reality}}} \\ &= 2 \frac{\sqrt{\ln 2}\sqrt{a^2L^2 + 3aL_{\text{end}}L + 3L_{\text{end}}^2} - \sqrt{3}L_{\text{end}}}{\sqrt{\ln 2}\sqrt{a^2L^2 + 3aL_{\text{end}}L + 3L_{\text{end}}^2} + \sqrt{3}L_{\text{end}}} \end{aligned}$$

When $L \rightarrow 0$ this result of $\text{FWHM}_{\text{Error}}$ can be below zero, which would suggest that the result is not an accurate measure of the true error. This is likely due to the process requiring a series expansion, at $x = 0$; as the series expansion is only an approximation of the target function. Since attaining error from the FWHM fails for small values of L an analysis using area was considered.

B.2 Bragg conditions

Proof of abbe limit from diffraction theory:

$$d \sin \alpha_n = n\lambda \quad (\text{B.1})$$

$$\sin \alpha_n = \frac{p_n}{f} \quad (\text{B.2})$$

$$p_n = \frac{n\lambda f}{d} \quad (\text{B.3})$$

$$d \leq = \frac{\lambda}{\sin \alpha_{\max}} \quad (\text{B.4})$$

$$d \leq = \frac{\lambda_0}{n \sin \alpha_{\max}} = \frac{2\lambda_0}{NA} \quad (\text{B.5})$$